Available online at www.sciencedirect.com
SCIENCE DIRECT®
ELSEVIER
Nuclear Instruments and Methods in Physics Research A 544 (2005) 300–309
NUCLEAR INSTRUMENTS & METHODS IN PHYSICS RESEARCH Section A
www.elsevier.com/locate/nima

Power plant conceptual design for fast ignition heavy-ion fusion

S. Medin[a,*], M. Basko[b], M. Churazov[b], P. Ivanov[a], D. Koshkarev[b], Yu. Orlov[c], A. Parshikov[a], B. Sharkov[b], V. Suslin[c]

[a]*Institute for High Energy Densities, RAS, Izhorskaya 13/19, 125412 Moscow, Russian Federation*
[b]*Institute for Theoretical and Experimental Physics, B.Cheremushkinskaya 25, 117259 Moscow, Russian Federation*
[c]*Keldysh Institute for Applied Mathematics, RAS, Miusskaya 4, 125047 Moscow, Russian Federation*

Available online 10 March 2005

Abstract

The concept of power plant for a fast ignition heavy-ion fusion (FIHIF) is being developed. The characteristics of super-high-energy-ion driver are described. The scenario of 750 MJ fusion yield target compression and detonation is evaluated. The data on reactor chamber response to energy fluxes generated by microexplosion are given. The energy conversion thermal scheme and power plant output parameters are presented.

PACS: 52.58.Hm; 28.52.Av; 52.57.Fg

Keywords: High-energy ion acceleration; Cylindrical target; Thin-liquid first wall; Reactor chamber response; Energy conversion system

1. Introduction

Principal aspects of heavy-ion IFE are determined mainly by the two design factors: the type of target drive and the blanket structurization. At the moment, the most advanced concept, HYLIFE-II [1,2] is based on the indirect drive of target and the thick liquid wall of blanket structure. The advantages of this concept are in mitigation of problems of driver–reactor chamber interface and reactor chamber materials. The difficulties involved are the organization of radiation-proof pocket of liquid jets and the demand of higher gain in target burn.

In Ref. [3,4], an alternative concept of heavy-ion IFE was considered. In this concept, the direct drive of cylindrical target in fast ignition mode and thin liquid wall design of blanket are accepted. This approach is characterized by a simple

*Corresponding author.
E-mail address: medin@ihed.ras.ru (S. Medin).

0168-9002/$ - see front matter © 2005 Elsevier B.V. All rights reserved.
doi:10.1016/j.nima.2005.01.224

driver–reactor chamber interface and a moderate value of demanded target gain.

The problems of concern in the fast-ignition heavy-ion fusion (FIHIF) concept are related to rigid physical conditions of fast ignition scenario implementation and heavy-ion driver length.

In this paper, new data on the target energy release and the reactor chamber response are given and output parameters of the FIHIF power plant are corrected.

2. Ground plan and high-power driver

In HIF, the ground plan of the power plant is mainly determined by the configuration of an accelerator system. The ground plan of FIHIF power plant is outlined in Fig. 1. The largest dimension of the ground plan is of the order of 10 km and corresponds to the length of the main linac. The other characteristic dimension is the diameter of storage and compression rings, which is equal to 1 km. The area occupied by the reactor and turbo-generator building, as well as cooling towers is within the same order of magnitude.

The driver is composed of the following major parts [4]. Ion sources for four Pt isotopes with plus and minus charge states are arranged in eight groups of 4 devices each. Funneling of equal number of positive and negative ions helps to compensate for the effects of space charge at the last stage of formation 20-kA-bunch current in ignition beam. In the low-energy linac tree, stepwise summation and acceleration of beams takes place. Then in the main linac the ion energy is increased to 100 GeV. After the main linac, the ions with different charges and masses are separated in 8 beams, which are compressed in two stages: in storage rings and in exit sections by the time-of-flight method. The final summation of 8 beams in an individual transfer line results in a single bunch of 0.2-ns-duration delivered to the compressed target. The preliminary compression of the target is accomplished by a hollow beam which carries only Pt^{+}_{192} ions. A hollow beam is supposed to be formed by fast (about ten revolutions per main pulse; see Ref. [5]) rotation of a 0.6–1.2 mm-focal-radius beam around the target axis. This beam is temporally profiled over the total duration of 75 ns with a maximum current of 1.6 kA. It is transferred to the reactor chamber through storage and compression rings.

The general parameters of the FIHIF driver are given in Table 1. Repetition rate of FIHIF driver is taken as 8 Hz, which provides 2 shots per second in each of 4 reactor chambers. The evaluated nominal driver efficiency is equal to 0.25. The operational characteristics of the driver equipment

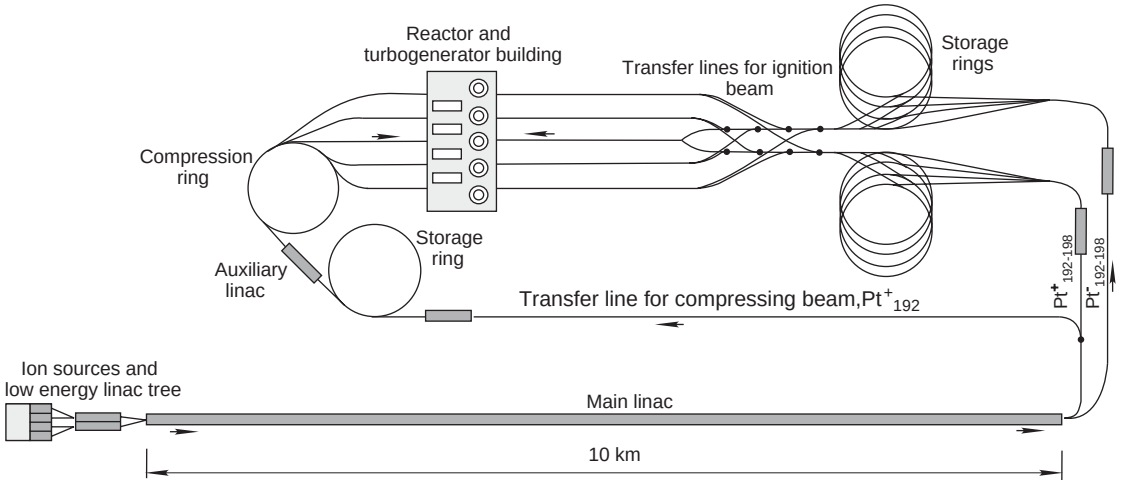

Fig. 1. Ground plan outline for FIHIF power plan.

Table 1
General parameters of FIHIF driver

Ions	$Pt^{+,-}_{192,194,196,198}$
Ion energy (GeV)	100.0
Hollow compressing beam	
Energy (MJ)	7.1
Duration (ns)	75 (profiled)
Maximum current (kA)	1.6
Rotation frequency (GHz)	1.0
Rotation radius (mm)	2.0
Spot radius (mm)	0.8
Ignition beam	
Energy (MJ)	0.4
Duration (ns)	0.2
Max. current (kA)	20
Spot radius (μm)	50
Linac	
Main linac length (km)	10.0
Repetition rate (Hz)	8.0
Driver efficiency	0.25

are feasible on the basis of today's development of acceleration technologies.

The problems of concern for FIHIF driver are generation of negative Pt ions, fine focusing of the ignition beam on 100-μm-diameter spot and too large length of the main linac.

3. Cylindrical target

The target design used here is based on detailed simulations in Ref. [6]. The DT fuel cylinder with a radius of 0.112 cm and a length of 0.71 cm is surrounded by a lead shell with a radius of 0.4 cm and a length of 0.8 cm (see Fig. 2). The target ends are sealed by thin (1 mm or less) walls of lead that can be easily penetrated by the igniting beam. The masses of fuel and lead are equal to 5.6 mg and 4.44 g, respectively. The length of the target is matched to the stopping range of 100 GeV Pt^{+}_{192} ions deposited by the compressing hollow beam.

The parameters of target compression and burn were determined in separate (1D for compression, and 2D for ignition) simulations [6]. The Rayleigh–Taylor instability at the compression stage is mitigated by finite density gradients; for more details see Refs. [6,7]. The compression results in the fuel density of 100 g/cm^3 and the DT fiber radius of 50 μm. Ignition of fuel is accomplished by the second beam. A burn wave propagates along the DT fiber with a velocity of 5×10^6 m/s. The burn fraction amounts to 0.39 providing a fusion energy of 750 MJ and a gain of 100. The lead plugs at target ends are expected to disturb its performance over a length of the order of the initial DT radius ~1 mm from each end; such disturbances can be compensated by increased target length.

The fusion energy is partitioned among 580 MJ in neutrons, 153 MJ in debris and 17 MJ in X-rays.

The rather high-energy fraction in debris is caused by X-ray energy conversion in the massive lead shell into its kinetic energy. X-ray radiation is

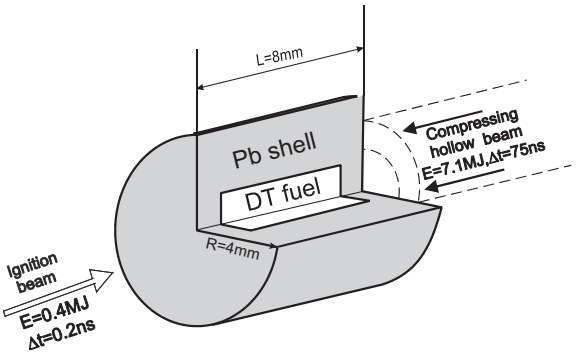

Fig. 2. Cylindrical target for FIHIF concept.

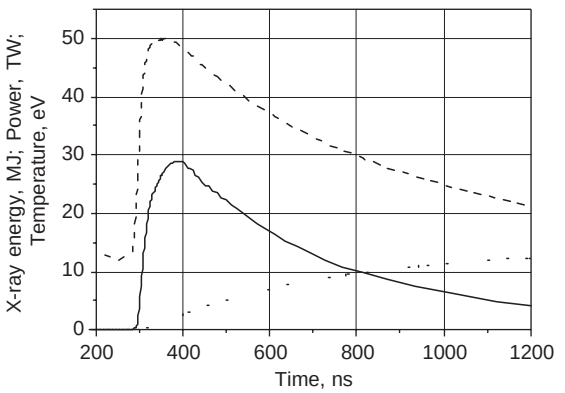

Fig. 3. Temporal profiles of X-ray characteristics for FIHIF cylindrical target. Dashed line: temperature, solid line: power, dotted line: energy.

originally absorbed by target material and then reradiated by lead plasma. This causes the decrease in X-ray temperature and delay and lengthening of the X-ray pulse. In Fig. 3, the profile of X-ray pulse is drawn. The duration of the pulse is very long and exceeds 0.7 μs; the mean X-ray temperature is equal to 30 eV.

The main concern for target ignition is related to the Rayleigh–Taylor instability at the final stage of fuel compression and confirmation of stable burn ware propagation based on multidimensional numerical simulation.

4. Reactor chamber

Because of high vacuum in the FIHIF reactor chamber, the first wall is exposed to extreme power fluxes. An ablation effect has to be used for protection of the first wall. Of the two basic designs, thick liquid wall and thin liquid wall, we choose the latter.

The general design of the reactor chamber is shown in Fig. 4. The cylindrically symmetrical chamber consists of the two sections: the upper smaller section, in which the target explosion takes place, and the lower section, in which sprayed jets of coolant are injected. The diameters of the sections are 8 and 16 m, respectively. Such a configuration of the chamber prevents an overpressurization after the microexplosion and provides high rate of vapor condensation on enlarged liquid surface of sprayed jets.

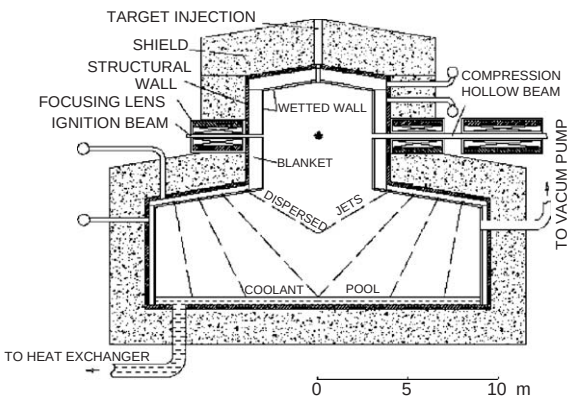

Fig. 4. Reactor chamber for FIHIF power plant.

The coolant is eutectic $Li_{17}Pb_{83}$. The coolant temperature of the first wall film is taken as 823 K. A saturation density of vapor of $10^{18}\,m^{-3}$ corresponds to this temperature [8]. Under this condition, the Pt ion beam is not deteriorated by an atmosphere in the reactor chamber.

The first wall and the blanket are of conventional design. The liquid film is formed at SiC porous wall. In the blanket, the tubing is made of vanadium alloy. The structural wall is manufactured of HT-9 steel. The dimensional structurization of the blanket design is given below in Section 6.

5. Reactor chamber response to X-rays and ion debris

An impact of the microexplosion on the chamber wall starts with X-ray deposition in liquid film. The X-ray radiation is characterized by an energy density of $Q = 8.5 \times 10^4\,J/m^2$ for $R = 4\,m$ at the equatorial plane of the fireball. An attenuation length in $Li_{17}Pb_{83}$ for average photon energy of 30 eV equals $10^{-7}\,m$.

Since the duration of radiation pulse is long enough, $t = 0.7\,\mu s$, evaporation of the coolant can be considered as a quasistationary heat wave propagating in the film. In this case, for evaluation of evaporated mass flow rate and recoil pressure we use the solution for variation of vapor parameters through Knudsen layer developed by Anisimov et al. in Ref. [9]. In this layer of a few mean free paths width, an isotropic distribution of evaporated atom velocities is established. In Ref. [9], by means of Boltzman's equation solution the equations of conservation of mass, momentum and energy are solved numerically for this layer involving a closing condition of equality of gas velocity to a sound velocity at the external boundary of the layer. For a given heat flux at liquid surface, all characteristics of evaporation wave for a number of substances are computed [9].

For heat flux of $1.2 \times 10^{11}\,W/m^2$, we take the following Anisimov's data for pure Pb as an upper estimate: evaporation temperature 5900 K, eva-

poration pressure at the liquid surface 700 bar and mass flow rate $6.9 \times 10^4\,\mathrm{kg/m^2\,s}$. Therefore, we expect that 9.6 kg of $Li_{17}Pb_{83}$ is evaporated as a result of X-ray deposition. The velocity of vapor expansion is evaluated from the energy balance as 10^3 m/s.

Now let us estimate the effect of debris arrival to the first wall after explosion. Since the mass of the target is much greater than that of the coolant atmosphere, the debris flow in the chamber after the microexplosion can be evaluated by classical Sedov solution [10] for isentropic expansion of perfect gas in vacuum. The asymptotics of this solution for large distances $R \gg r$ (where r is initial radius of microexplosion fireball) describes the propagation of the expansion front with a constant velocity $U = (10E_d/(3M))^{0.5}$, where E_d is the debris energy and M is the mass of the target. So the debris front arrives at the first wall of the reactor chamber in time $R/U = 3.5 \times 10^{-5}$ s. During this time interval, the vaporized coolant layer expanding into the chamber cavity with the velocity of 10^3 m/s, passes the distance 3.5 cm from the wall. The average density of this vapor layer is $\rho_v = 1.3\,\mathrm{kg/m^3}$. The interaction of the debris flow and the vapor layer is determined by the stopping range of 80 keV ions in the dense vapor. The Bethe–Bloch rate of debris energy losses [11] for this case is approximately equal to $20\,\mathrm{GeV/g/cm^2}$, so the stopping range is equal to 3.5 μm, i.e. much smaller than the vapor layer. Hence all ions are absorbed in this thin layer. Therefore, it can be supposed that evaporated coolant is additionally superheated by debris ions. The evaluated resulting temperature of vapor amounts to 38 eV ($\approx 3.5 \times 10^5$ K). The process of additional vaporization and condensation is considered to start with this initial temperature of vapor.

The evaporation–condensation processes, we describe by kinetic relationships [12] in the same way as in Ref. [4]. We suppose that droplets of dispersed jets in the lower-chamber volume (see Fig. 4) provide needed value of condensation surface ($4.5 \times 10^4\,\mathrm{m^2}$ for droplets with total mass of 7000 kg per shot). In the simulation procedure, the condensation at the dispersed jets droplets is switched on at the time of 1 ms, when expanding vapor spreads in the lower part of the reactor chamber. Before this, the condensation takes place only at the first wall of the upper part of the reactor chamber. The results of computation of condensation are shown in Figs. 5 and 6. The condensation process has two distinctive phases. In the first phase, the additional vaporization occurs, while the vapor temperature intensively decreases. The sharp drop off in vapor density profile in Fig. 5 is produced by an instantaneous increase in the condensation surface contributed by the dispersed jets droplets. The maximum mass of the evaporated coolant is 15 kg. At the time of 10^{-8} s, the regime of vapor cooling is changed. The condensation prevails vaporization and the rate of

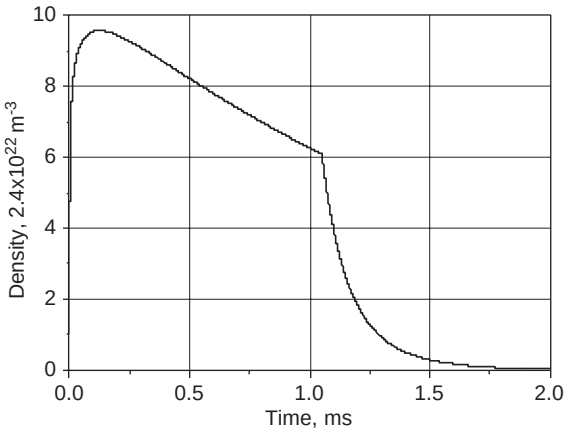

Fig. 5. Vapor density temporal variation in reactor chamber after the shot.

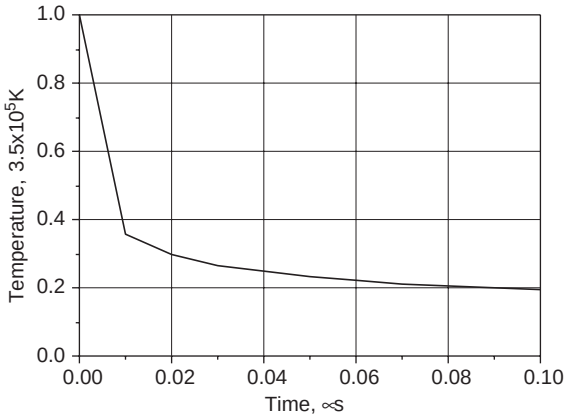

Fig. 6. Vapor temperature temporal variation in reactor chamber after the shot.

temperature decrease sharply falls. The vapor density practically reaches the saturation value at 0.017 s. This indicates that the condensation process would not limit a repetition rate of shots. Apparently, the actual limitation will be a rate of liquid droplets clean-up. In the case of free gravity precipitation, the repetition rate does not exceed 2 Hz.

6. Neutron heating of blanket

The blanket design is presented by a multi-layer cylinder, the structure of which is given in Table 2. Blanket and structural wall thickness is equal to 52 cm. We numerate blanket zones and inner radii from the surface of liquid protecting layer.

For evaluation of neutron energy deposition in the blanket, it was supposed that neutron irradiation is spherically symmetrical with the total energy of the pulse of $E_n = 580$ MJ. The neutron source, generated in DT-reaction, is presented in Fig. 7. The neutron spectrum is evaluated by stationary calculations with the use of MCNP code [13] in spherical approximation for the moment of central peak of neutron pulse. The average neutron energy is equal to 12.2 MeV.

Two-dimensional calculations of neutron transport in the blanket with the use of MCNP code resulted in high-energy release in the materials. Tritium breeding ratio (TBR) for this blanket is equal to 1.112, and blanket multiplication factor is evaluated by the value of 1.117. So the total energy release per one shot is equal to 818 MJ.

The duration of neutron pulse is of the order of 1 ns. This means that the isochoric heating of the blanket structure takes place at the initial stage. For

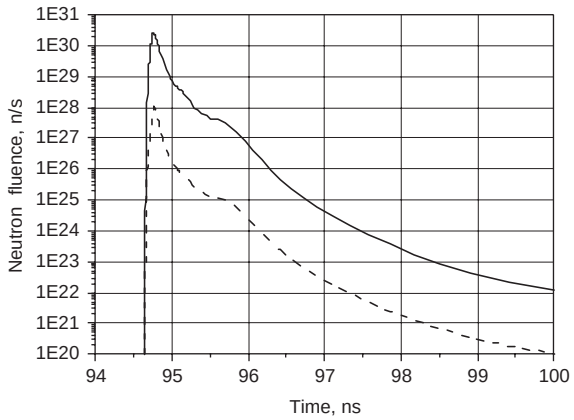

Fig. 7. Neutron pulse of the FIHIF target microexplosion. Solid line: 14 MeV; dotted line: 2.45 MeV.

Table 2
Blanket structure and energy deposition in the zones

Zone	Matter	Radius (cm)	Energy (MJ)	Temperature rise (K)
1	PbLi	400	6.9	13
2	SiC + PbLi	400.2	35.7	5.1
3	PbLi	401	241	11.1
4	V4Cr4Ti	407	8.4	2.8
5	PbLi	407.4	163.7	7.3
6	V4Cr4Ti	413.4	5.3	1.7
7	PbLi	413.8	92.9	4
8	V4Cr4Ti	419.8	2.8	0.9
9	PbLi	420.2	48.1	2
10	V4Cr4Ti	426.2	1.5	0.5
11	PbLi	426.6	22.6	0.9
12	V4Cr4Ti	432.6	0.7	0.2
13	PbLi	433	11.1	0.4
14	V4Cr4Ti	439	0.3	0.1
15	PbLi	439.4	5	0.2
16	V4Cr4Ti	445.4	0.4	0.05
17	HT-9	446.4	1	0.01
18	Concrete	452	—	—

Table 3
Properties of reactor chamber materials

Parameter	LiPb	SiC + LiPb	VCrTi	HT9	Concrete
ρ (kg/m^3)	9500	4800	6100	7800	1600
K (Gpa)	35	81.5	280	158	20
G (Gpa)	0	55	42.7	77.6	17
Y (Mpa)	—	35	223	422	—
Γ	2.7	2	1.23	2	2
c (m/s)	1922	4120	6780	4500	3535
Cp (J/(kg K))	188	660	546	700	840
λ (W/(m K))	16	10.9	34	33	1.28

evaluation of material loading, we solve 1D cylindrically symmetrical equations of conservation of mass, momentum and energy in the equatorial plane of the fireball. The Lagrangian description is used and the radial dimension of the numerical particle is taken as 0.5 mm. The computational interval includes blanket, structural wall and concrete shield whose widths are equal to 0.464, 0.056 and 2.5 m, respectively. Free adiabatic boundary conditions were used. Initial distributions were uniform for all the parameters except for internal energy which was determined from neutronics computations. The material properties are given in Table 3.

The data for solid materials, silicon carbide, vanadium alloy and stainless steel, are given by Zinkle in Ref. [14]. The eutectic $Li_{17}Pb_{83}$ properties are taken from Ref. [15]. The density ρ, bulk modulus K, specific thermal capacity C_p and thermal conductivity λ are computed for the SiC porous wall filled by the eutectic by means of mixture formulae at 0.5 weight ratio; the shear stress modulus G and yield stress Y are projected from Zinkle data. The equation of state is taken in the Mie–Gruneisen form. The Gruneisen coefficient Γ is projected as 2 for SiC porous wall, stainless steel and concrete.

Neutron heating generates a pressure/stress pulse which travels across the blanket and refracts at the contact surfaces. In Fig. 8a, pressure radial distribution in the blanket and the structural wall is drawn for different times. Fig. 8b presents a scaled structure of the blanket and the structural wall. The right boundary is the contact interface between stainless steel and concrete. The development of the pressure pulse with compression and release phases is seen. The pulse is partially reflected from the concrete. The reflection coefficient is computed from Table 3 data as $R =$

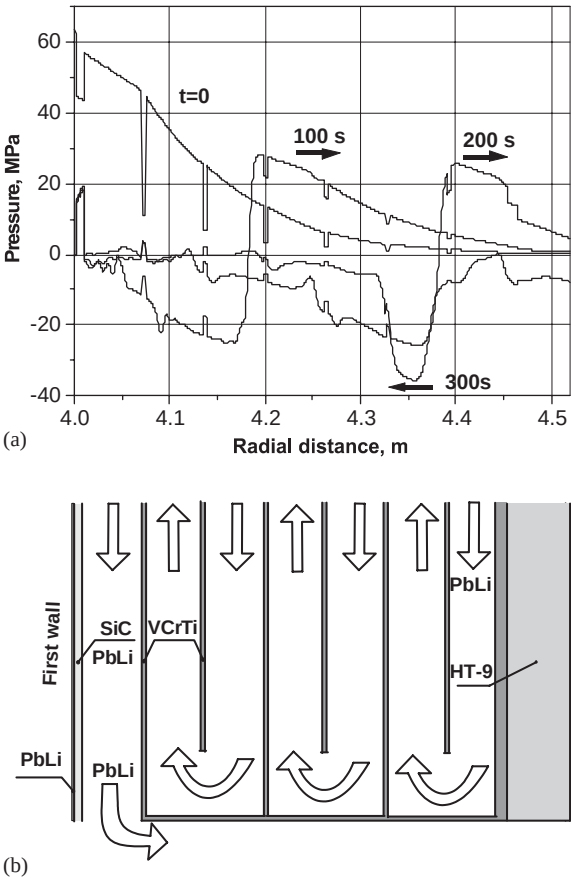

Fig. 8. (a) Pressure distribution in the FIHIF reactor chamber blanket and the structural wall at various times. (b) Configuration of the design.

$(\rho_1 c_1 - \rho_2 c_2)/(\rho_1 c_1 + \rho_2 c_2) = 0.72$. At $t = 0$, the shape of the pressure distribution corresponds to penetration length of neutrons in coolant. In the walls, the sharp downfalls of pressure occur because of smaller deposited energy density and mass density than those in coolant. Transformation of the pulse in time has general features of analytical solution for exponential energy deposition in uniform half-space [16]. Negative pressure in developed pulse has an amplitude of -25 MPa. This may cause cavitation in coolant. High-frequency pulsations of smaller amplitude around the walls reflect loading and release of the wall material in coolant.

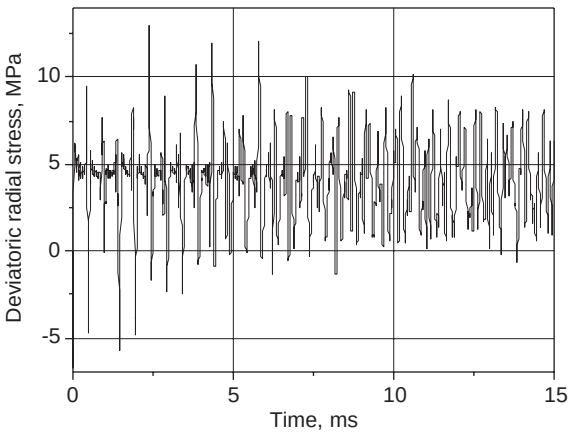

Fig. 9. Deviatoric stress temporal profile for the first vanadium alloy wall inside the blanket after the shot.

In Fig. 9, the oscillogram of deviatoric radial stress S_{rr} in the first vanadium alloy wall is presented. The base level of S_{rr} is positive, which means that material is compressed on average. The main pulsations having negative and positive amplitudes are attributed to the neutron loading pulse reflections within the blanket and the structural wall. The frequency of main pulsations of S_{rr} is 2.3 kHz. The maximum value of S_{rr} amounts to 11 MPa, which is much less than the elastic limit $Y/\sqrt{3} = 129$ MPa. The main pulsation is modulated by low frequency, which can be caused by refracted pulse reflection in concrete.

The problems of concern still to be analyzed are the material degradation due to neutron radiation, fatigue under pulse loading and cavitation in coolant.

7. Energy conversion and balance of plant system

The energy conversion system consists of three loops (Fig. 10). The coolant of the second loop is sodium. The third loop is a steam turbine cycle. The key parameter of the system is the maximum temperature of $Li_{17}Pb_{83}$ at the outlet of the reactor chamber. It is taken as 823 K. The inlet temperature of the eutectic is equal to 623 K. The

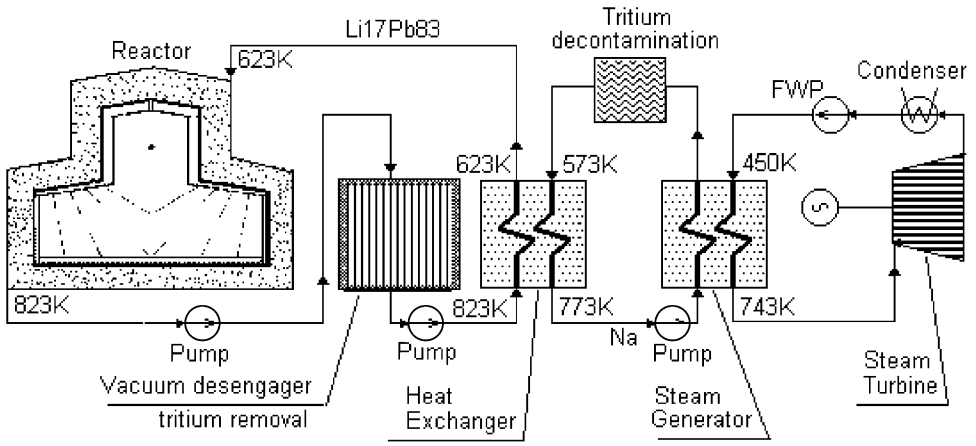

Fig. 10. Thermal Scheme for FIHIF power plant.

Table 4
Parameters of thermal loops of FHIF power plant

First loop	
Coolant	LiPb
Mass flow rate (kg/s)	13063
Pump power (kW)	11584
Second loop	
Coolant	Na
Mass flow rate (kg/s)	6402
Pump power (kW)	3768
Steam cycle	
Mass flow rate (kg/s)	548.7
Inlet pressure (Mpa)	18
Superheat pressure (Mpa)	3
Condenser pressure (Mpa)	0.009
Turbine efficiency	0.875
Steam cycle efficiency	0.417
Reactor	
Fusion power (MW)	1500
Driver power (MW)	60
Neutron power ratio	0.773
Blanket multiplication	1.117
Power plant	
Thermal efficiency	0.407
Net efficiency	0.374
Net power output (MW)	626

temperature drop at the walls of the intermediate heat exchanger is determined as 50 K. So the inlet and outlet temperatures of sodium in the intermediate heat exchanger are 573 and 773 K, respectively. In Table 3 the mass flow rate and the pump power for liquid metal coolants are given (Table 4).

The steam cycle is configured with a reheat. The initial steam temperature and the reheat temperature are equal to 743 K. The minimum temperature drop of 40 K of the steam generator heating walls is realized at the outlet because of the isothermal segment of vaporization in the temperature–enthalpy diagram. The temperature of feeding water is computed as 450 K. The efficiency of the steam cycle equals 0.407. Taking into account the driver efficiency, the target gain and the blanket multiplication for the fusion power of 1500 MW, we obtain a net efficiency of the plant of 0.373 and net power per one reactor of 626 MW.

8. Conclusions

The FIHIF physical scenario, based on the high-energy ion beams drive of a cylindrical target involves a realistic acceleration technology and a simple target design although a large site for the driver, precise target–beams interface and reliable compression-detonation of DT fuel are to be provided.

Wetted first wall and a minimum number of ports for beam injection allow to follow a conventional design of the reactor chamber. The configuring of the reactor of two sections gives a possibility to increase the rate of vapor condensation and to reduce the vapor pressure loading. The problems of vapor fog in the chamber and pressure-stress pulsations in the blanket are a major concern of the reactor.

The materials limitations and tritium contamination of coolant determine thermodynamics of the thermal scheme. The balance of plant is highly influenced by the driver energy consumption. Improvement in material characteristics and the driver–target performance is needed to increase the efficiency of the power plant.

Acknowledgments

This work is sponsored by the Human Capital Foundation under contract N32. It is supported in part by the Complex Program on Basic Research of the Presidium of Russian Academy of Sciences N17.

References

[1] J.D. Lindl, et al., Plasma Phys. Contr. Fusion 45 (2003) A217.
[2] W.R. Meier, et al., Fusion Eng. Des. 62–63 (2003) 577.
[3] S.A. Medin, et al., Laser Part. Beams 20 (2002) 419.
[4] S.A. Medin, et al., Fusion Sci. Technol. 43 (2003) 437.
[5] M.M. Basko, et al., Phys. Plasmas 11 (2004) 1577.
[6] M.M. Basko, et al., Laser Part. Beams 20 (2002) 411.
[7] M.M. Basko, et al., Phys. Plasmas 9 (2002) 1348.
[8] R.W. Moir, Fusion Eng. Des. 32–33 (1996) 93.
[9] S.I. Anisimov, et al., Action of High Power Radiation on Metals, Nauka, Moscow, 1970 (in Russian).

[10] L.I. Sedov, Methods of Similarity and Dimension in Mechanics, GITTL, Moscow, 1954 (in Russian).
[11] B. Rossi, High Energy Particles, Prentice-Hall, Englewood Cliffs, NJ, 1952.
[12] V.P. Isachenko, Heat Transfer in Condensation Processes, Energia, Moscow, 1977 (in Russian).
[13] GROUP-6, MCNP—A General Monte Carlo Code for Neutron and Photon Transport, LA-7396-m revised, Los Alamos National Laboratory, April 1981.
[14] S.J. Zinkle, Status of Recent Activities by the APEX Material Group, APEX Study Meeting, Sandia National Laboratories, 1998, p. 18.
[15] V.N. Mikhailov, et al., Lithium in Fusion and Space Power in 21 Century, Nauka, Moscow, 1999 (in Russian).
[16] J.C. Bushnell, D.J. McCloskey, J. Appl. Phys. 39 (1968) 5541.